Transient thermal flow in a U-Bend and its influence on wall thermal stress

Wendi Liu, Alex Skillen, Małgorzata J. Zimoń, Robert Sawko, Charles Moulinec and David R Emerson

Published version information

Citation: W Liu et al. 'Transient thermal flow in a U-Bend and its influence on wall thermal stress.' Computational Thermal Sciences: An International Journal, vol. 13, no. 4 (2021): 1-20.

DOI: 10.1615/ComputThermalScien.2021035729

Transient Thermal Flow in a U-Bend and its Influence on Wall Thermal Stress

Wendi Liu [a, *], Alex Skillen [a, b], Małgorzata J. Zimoń [c], Robert Sawko [c], Charles Moulinec [a] and David R Emerson [a]

a. *Scientific Computing Department, Science and Technology Facilities Council, Daresbury Laboratory, Warrington WA4 4AD, UK;*
b. *Department of Mechanical Aerospace and Civil Engineering; School of Engineering, The University of Manchester, UK;*
c. *IBM Research UK, Daresbury Laboratory, Warrington WA4 4AD, UK.*

[*]Corresponding author. Email: wendi.liu@stfc.ac.uk

ABSTRACT

The present study focused on the propagation of a hot thermal transient through a U-Bend, and the resulting thermal stresses this causes. The flow conditions are fully turbulent in a mixed convection regime. A coupled framework has been used to simulate the 3-D conjugate heat transfer between the fluid and solid domains, and subsequently compute the thermal stress within the solid domain. An empirical model is then used for the fatigue life prediction. Highly complex flow evolution has been observed. Significantly, the reversal of the Dean vortex pair due to buoyancy has been identified. This reversal causes steep wall temperature gradients, increases the thermal stress at the front and back part of the two bends, and generates a large stress region at the bottom of the near-horizontal section, which leads to a fatigue life reduction of the U-bend.

Keywords: *Conjugate heat transfer*; *von-Mises Stress*; *Coupled simulation*.

1. Introduction

Predicting thermal stress is a key element in the design of pipework for nuclear power plants. The time-averaged and peak thermal stresses during different operating cycles are useful for predicting the cumulative fatigue damage of a pipe (Schwartz, 1982, Fatemi and Yang, 1998). However, simulating pipe thermal stresses is challenging due to coupled nature of the governing equations (Marugán-Cruz *et al.*, 2016). Many researchers have contributed to the simulation of stresses for straight pipes (Flores *et al.*, 2014, Rodríguez-Sánchez *et al.*, 2014). In contrast to straight pipes, the heat transfer of a U-bend exhibits some unique phenomenon due to its shape, which makes the thermal stress simulation more challenging. One aspect is the appearance of Dean vortices. They are counter-rotating vortices created by the flow around bends due to the local imbalance between centripetal forces and the opposing pressure gradient. These secondary flows occur in many industrial applications and can have a significant impact on heat and mass transfer (Vashisth *et al.*, 2008, Noorani *et al.*, 2013, Giannakopoulos *et al.*, 2017). Skillen *et al.* (2020) also indicated that there is a significant impact on the thermal stratification from the secondary flow, such as Dean vortices. The dynamics of a hot thermal transient propagating through pipe bends is particularly relevant to the nuclear industry. In mixed convection conditions (relevant to the passive safety case of nuclear reactors), thermal transients can significantly affect the Dean vortices, potentially leading to a reversal of the secondary flow (Viollet, 1987). Skillen *et al.* (2020) proposed a mechanism by which this Dean vortex reversal occurs; the thermal inertia of the wall causes near-wall fluid to remain at a lower temperature than that away from the wall. This generates a baroclinic torque, resulting in a buoyancy-induced secondary flow of the opposite direction to that of the Dean vortices. The propagation of a transient thermal flows can also generate stratified layers and large buoyancy-induced recirculation regions. This phenomenon has been reported by Viollet (1987), who carried out a series of simulations on the U-bend with a linear ramp of the inlet fluid temperature. He concluded that the thermal

stratification tends to appear at low Froude number and Reynolds number conditions. Both these phenomena add significantly to the complexity, relative to the straight pipe.

Stratification of a thermal transient can lead to steep temperature gradients, in both fluid and solid domains, that can adversely affect the pipe wall by raising the thermal stress. Therefore, accurately predicting the thermal stress of a U-bend is an important capability in the design of pipework. Prevéy (1981) studied the macroscopic residual stress distributions of a U-bend using site data. Cheng and Finnie (1996) carried out a stress and fatigue analysis of U-bend steam generator tubes based on available U-bend data where fatigue failure had occurred. They observed that the maximum stress of the U-bend is close to the cyclic yield stress, where Goodman's straight-line analysis (Goodman, 1919) provided a reasonable approach for predicting its fatigue life. Attia (2006) carried out an experiment on the long-term fretting wear of a full-scale U-bend tube of steam generators and established a framework on the fretting risk management. However, any interaction between the thermal fluid and the stress of the U-bend tube was not considered in their research.

In this study, a coupled framework has been used to model the 3-D incompressible Navier-Stokes equations with the Unsteady Reynolds Averaged Navier-Stokes (URANS) equations, and linear thermo-elastic formulations. Conjugate heat transfer (CHT) between the fluid and solid walls is also considered. The aim of this paper is to assess the influence of the secondary flow reversal has upon the stresses within a u-bend pipe wall.

This paper is structured as follows: the problem formulation used in the present study is presented in the next section, followed by the results and discussion. Finally, some conclusions are drawn.

2. Problem Formulation

2.1.Governing Equations and Numerical Schemes

The simulations for the present study are carried out using a coupled framework, as shown in Figure 1. The framework employs three simulation domains (i.e. Finite Volume (FV) fluid domain for the simulation of the fluid flow inside the U-bend pipe, FV structure domain for the simulation of the heat transfer of the U-bend wall and Finite Element (FE) structure domain for the simulation of the thermally-induced stress/fatigue of the U-bend wall) across two codes, which are Code_Saturne version 5.0 (Fournier *et al.*, 2011) and FEniCS version 2019.1.0 (Alnæs *et al.*, 2015). Three sets of meshes are used for the simulation, which are hexahedral mesh for the FV fluid domain, hexahedral mesh for the FV structure domain, and tetrahedral mesh for the FE structure domain. Conformal hexahedral meshes are used between FV fluid and FV solid domains for the U-bend wall. Non-conformal meshes are used between the FV and FE structure domains. Conjugate heat transfer simulations are performed with Code_Saturne as shown in the left-hand part of Figure 1. The coupling between the FV fluid and FV solid domains is accounted for internally within Code_Saturne by enforcing consistent temperature and heat flux between the domains, using the Code_Saturne's PLE library (Fournier, 2020). The fluid flow is governed by the incompressible URANS equations. Turbulence closure is achieved through the use of the Elliptic Blending Reynolds-Stress Model (EBRSM) (Manceau and Hanjalić, 2002). As a low Reynolds number model, EBRSM does not need to apply any wall functions on the near-wall modelling and has the best performance on pipe bend simulations compared with other low Reynolds number URANS models (Tunstall *et al.*, 2016). The turbulent heat fluxes are modelled by the Generalised Gradient Diffusion Hypothesis (GGDH) (Daly and Harlow, 1970, Ince and Launder, 1989) approach. The density variation of the water is up to 8.4% of its original density for a typical case in the present study,

as presented in the following sections. Since the focus of this study is the thermal stress rather than the fluid flow, the Boussinesq approximation is used and the impact of the density variation is seen as secondary, and is thus neglected. Buoyancy is accounted for through a Boussinesq approximation in both the gravity source term and the turbulence production (Viollet, 1987) for the fluid simulations.

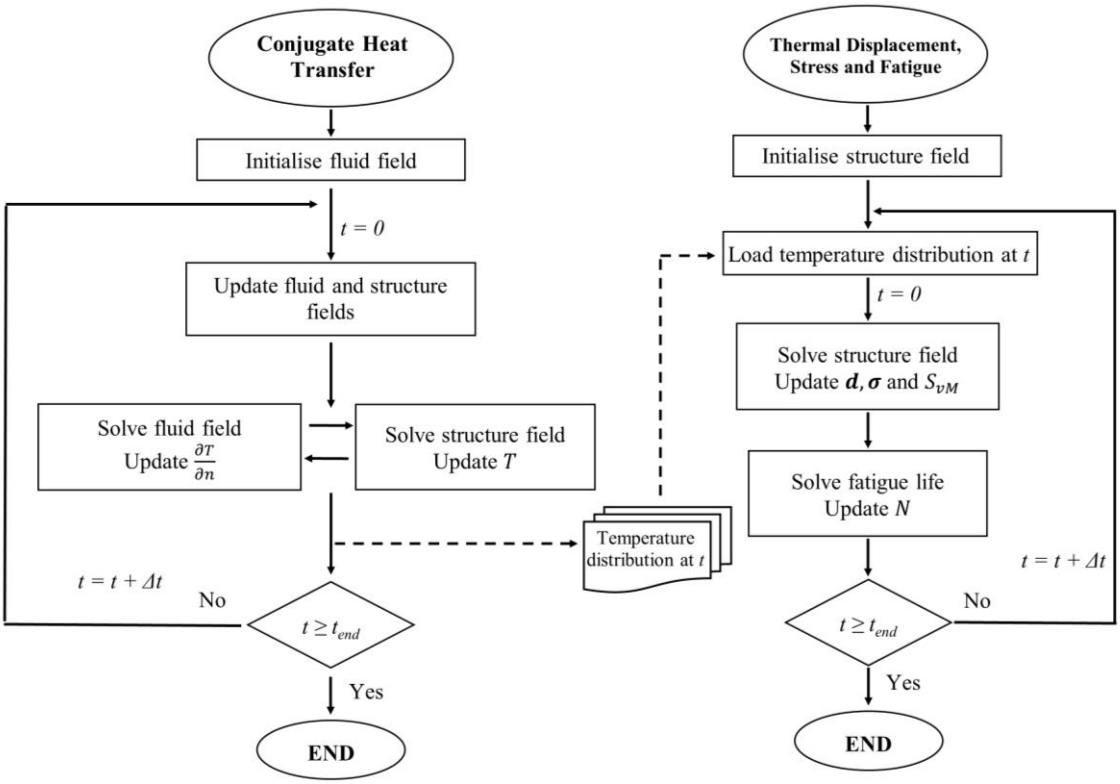

Figure 1. Flow chart of the simulation framework.

The Thermal Displacement, Stress analysis, and Fatigue life prediction (TDSF) of the U-bend are performed on the FE structure domain, as shown in the right-hand part of Figure 1. Linear thermo-elastic formulations are implemented within our customised FEniCS solver. Based on the virtual work principle (Bleyer, 2018), the continuum mechanics variational formulation is to find $\boldsymbol{d} \in \boldsymbol{\Theta}$ such that

$$\int_{\boldsymbol{\Omega}} \langle \boldsymbol{\sigma}(\boldsymbol{d}, T), \boldsymbol{\varepsilon}(\delta \boldsymbol{d}) \rangle \, d\boldsymbol{\Omega} = \int_{\boldsymbol{\Omega}} \delta \boldsymbol{d} \cdot b \, d\boldsymbol{\Omega} + \int_{\Gamma} \delta \boldsymbol{d} \cdot \widehat{ta} \, d\boldsymbol{\Gamma}, \quad \forall \delta \boldsymbol{d} \in \boldsymbol{\Theta}, \tag{1}$$

where $\boldsymbol{d}$ is the displacement vector, $\delta \boldsymbol{d}$ is the displacement increment, T is the temperature distribution, $\boldsymbol{\Theta}$ denotes the displacement admissible function space, $\boldsymbol{\Omega}$ is the physical domain, $\boldsymbol{\Gamma}$ is the boundary of the domain, b is the applied mechanical volume load, $\boldsymbol{\sigma}$ is the stress tensor, and $\widehat{ta}$ is the prescribed traction on the solid boundary. The strain tensor, $\boldsymbol{\varepsilon}(\delta \boldsymbol{d})$, is determined from

$$\boldsymbol{\varepsilon}(\delta \boldsymbol{d}) = \frac{1}{2}(\delta \boldsymbol{d} + (\delta \boldsymbol{d})^T), \quad in \, \boldsymbol{\Omega}, \tag{2}$$

and the stress tensor, $\boldsymbol{\sigma}$, is calculated as follows:

$$\boldsymbol{\sigma}(\boldsymbol{d}, T) = \langle \boldsymbol{C}, (\boldsymbol{\varepsilon}(\delta \boldsymbol{d}) - \boldsymbol{\varepsilon_t}) \rangle = \lambda tr\big(\boldsymbol{\varepsilon}(\delta \boldsymbol{d})\big)\boldsymbol{I} + 2\mu \boldsymbol{\varepsilon}(\delta \boldsymbol{d}) - \boldsymbol{\varepsilon_t}, \tag{3}$$

where $\boldsymbol{C}$ is the constitutive tensor, $tr(a)$ denotes the trace of any matrix a, $\boldsymbol{I}$ is the identity matrix, and λ and μ are the Lamé coefficients. The thermal strain tensor, $\boldsymbol{\varepsilon_t}$, is calculated as

$$\boldsymbol{\varepsilon_t} = \alpha_t(3\lambda + 2\mu)(T - T_0)\boldsymbol{I}, \quad in \, \Omega, \tag{4}$$

where α_t is the thermal expansion coefficient and T_0 is the reference temperature. The equilibrium equation, which is used to complete equation (1), is expressed as

$$\rho_s T_0 \dot{s} + \nabla \boldsymbol{q} = 0, \tag{5}$$

where ρ_s is the density of the solid material and $\dot{s}$ is the rate of change of entropy per unit mass.

The heat flux, $\boldsymbol{q}$, is obtained from the isotropic Fourier law

$$\boldsymbol{q} = -k\nabla T, \tag{6}$$

where k is thermal conductivity. With equations (1) to (6), the thermally-induced displacement and stress can be obtained. The displacement is non-dimensionalised as $\widetilde{\boldsymbol{d}} \equiv \boldsymbol{d}/D$, where D is the pipe's diameter.

The TDSF solver employs empirical equations to predict the fatigue life of the U-bend, following the procedure of Cheng and Finnie (1996). The localised purely alternating stress at the i^{th} element, σ_{pa}^{i}, and the localised cycles to failure at the i^{th} element, N^{i}, are determined from the following expression (Jacko, 1983)

$$\log \sigma_{pa}^{i} = A - B \log N^{i}, \tag{7}$$

where $A = -2.982$ and $B = 0.096$. The mean stress effect on the fatigue life of the U-bend under thermal stress can be expressed by the modified Goodman line (Goodman, 1919, Cheng and Finnie, 1996) as

$$\frac{\sigma_{a}^{i}}{\sigma_{pa}^{i}} + \frac{\sigma_{m}^{i}}{\sigma_{u}} = 1, \tag{8}$$

where σ_{a}^{i} is the localised stress combining the mean and purely alternating stresses, σ_{m}^{i} is the localised mean alternating stress, and σ_{u} is the ultimate strength of the U-bend with the value of 5.82×10^{8} Pa (Cheng and Finnie, 1996). The localised cycles to failure at the ith cell can be obtained by combing equations (7) and (8) as

$$N^i = 10^{A/B}\left[\frac{1-\frac{\sigma_m^i}{\sigma_u}}{\sigma_a^i}\right]^{1/B} . \quad (9)$$

As the thermal displacements are less than 9% of the pipe diameter (as presented in Section 3.3) and have limited influence on the CHT simulation, a one-way coupling method is used for the framework. During the simulation, the temperature distribution of the U-bend wall obtained from the CHT simulations is passed to the TDSF solver through file I/O. The TDSF solver reads in the data of temperature distribution at the present time step that based on the mesh of the FV structure domain. To ensure a consistency interpolation of the temperature distribution between non-conformal FV and FE structure meshes, an interpolation polynomial in the Lagrange form (Langtangen, 2012) is used in the TDSF solver as

$$T(\boldsymbol{x_{FE}}) = \sum_{j=1}^{n} T(\boldsymbol{x_j})\phi_j(\boldsymbol{x_{FE}}), \quad (10)$$

where, $\boldsymbol{x_{FE}}$ is the 3-D coordinate of an arbitrary element node of the FE structure mesh, n is the total number of cells of the FV structure mesh, $\boldsymbol{x_j}$ is the 3-D coordinate of the centre of the cell j of the FV structure mesh and $\phi_j(\boldsymbol{x_{FE}})$ is the Lagrange basis polynomials. After the interpolation, the temperature distribution at the present time step based on the FE structure mesh is applied to the FE structure domain as a volumetric source term for the TDSF simulations.

2.2.Geometry and Mesh

The geometry of the U-bend is shown in Figure 2. The length of both vertical sections is $10D$, while the radius of curvature of both elbows is $1.5D$. The near-horizontal section is $6D$ in length, with a slope of 1% to approximate the pipework of the Superphénix reactor (Viollet,

1987, Skillen *et al.*, 2020). The wall thickness is $0.05D$. As shown in Figure 2, the origin point of the system, o, is located in the centre of the inlet boundary, i.e. the top of the left hand side of the vertical section of the pipe, with a global Cartesian frame of reference, $x - y - z$. In this study, a mesh comprising approximately 4M and 0.5M cells in the FV fluid and FV solid domains, respectively, has been employed. Tests were performed with meshes comprising 1.2M FV fluid cells and 0.3M FV solid cells, and no appreciable differences were observed in the wall temperatures (Zimoń *et al.*, 2020). The TDSF simulation employs 0.5M tetrahedral elements in the FE solid domain. By increasing the tetrahedral elements to 4.6M for the mesh sensitivity test, the TDSF simulation gives the same results on the wall thermal displacements. TDSF simulations in the following sections were carried out by 0.5M elements.

2.3.Initial and Boundary Conditions

A no-slip condition for the velocity and a zero-gradient Neumann condition for the pressure at the interface between the fluid and solid domains of the CHT simulation have been enforced in the present study. At this interface, consistency in both the heat flux and temperatures is also enforced. A zero gradient Neumann condition is applied for the temperature at the U-bend external wall.

The fluid flow is initialised by conducting an isothermal URANS computation at T_0. These results are used as the initial condition of the simulation at a dimensionless time $\tilde{t} \equiv Ut/D = 0$, where t is the time and U is the bulk flow velocity. The temperature of the inlet thermal transient linearly increases with time until reaching its final value $T_1 = T_0 + \Delta T$ with a total temperature difference of ΔT at $\tilde{t} = 7.5$. For $\tilde{t} > 7.5$, the temperature of the inlet fluid remains as T_1. The diameter of the pipe, D, is determined by T_0 and ΔT in the present study. A Dirichlet condition is applied to the pressure and a zero-gradient Neumann condition is applied for all other variables at the outlet of the U-bend.

In the present case, no mechanical volume load or prescribed traction are applied. The stress-free reference temperature, T_0, is set to be constant throughout the pipe in the TDSF simulations. Point-based displacement constraints at both inlet and outlet of the pipe-wall have been implemented, as shown in Figure 2. These two constraints are equivalent to the pipe being pinned to these locations so that to prevent the left and right vertical sections from diverging from one another but allow the solid structure to expand in response to the temperature distribution.

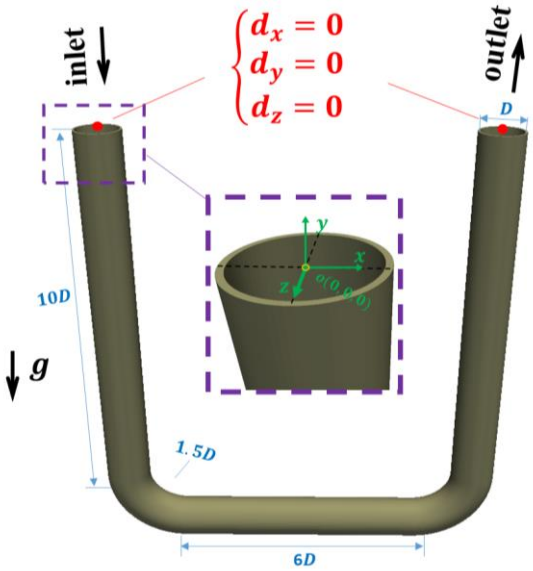

Figure 2. Schematic diagram of the geometry and boundary conditions.

2.4.Study Parameters

The present study focuses on the influence of a hot thermal transient to the U-bend where the inlet temperature increases with a linear ramp as indicated in the section of Initial and Boundary Conditions. The properties of the fluid flow (i.e. water in the present study) are defined by the dimensionless parameters of the Reynolds number

$$Re \equiv \frac{UD}{\nu} = 10{,}000, \tag{11}$$

the reduced Froude Number

$$Fr \equiv \frac{U}{\sqrt{g\beta\Delta TD}}, \tag{12}$$

and Prandtl number

$$Pr \equiv \frac{\nu}{\alpha} = 6, \tag{13}$$

where ν, g, α and β are kinematic viscosity, gravitational acceleration, thermal diffusivity and thermal expansion coefficient, respectively. The values of the Reynolds number and Prandtl number are based on the work of Viollet (1987), which are for mixed convection, fully-turbulent flow conditions. Three Froude numbers (i.e. $Fr = 0.670$, 0.814 and 0.913) are adopted for the present study to investigate how much of an influence changing the flow regime has on the thermal stresses. The temperature difference, ΔT, is chosen as $311.15\ K$ at $Fr = 0.670$ as suggested by Durmayaz and Yavuz (2001) with a reference temperature, $T_0 = 562.15\ K$ based on the study of Nair and Gopal (1987), Green and Hetsroni (1995) and Durmayaz and Yavuz (2001). Froude number changes are achieved by varying ΔT. The flow properties of the present study with $Fr = 0.670$ are listed in Table 1.

Table 1

Properties of water under the present working condition and the diameter of the U-bend pipe (Blumm and Lindemann, 2003, Engineering, 2003, Engineering, 2004).

Property	Unit	Value
Density	kg/m^3	667.09
Kinematic viscosity	m^2/s	1.17×10^{-7}
Thermal expansion coefficient	1/K	2.21×10^{-3}
Thermal diffusivity	m^2/s	1.27×10^{-7}
Thermal conductivity	W/(m·K)	0.68
Gravitational acceleration	m/s^2	9.81
Flow velocity	m/s	7.57×10^{-2}
Diameter of pipe	m	1.55×10^{-2}

The rate of conductive heat flow between the fluid and solid domains are determined by the ratio of thermal diffusivities

$$\frac{\alpha_s}{\alpha_f} = 144.8, \tag{14}$$

and the ratio of thermal conductivities

$$\frac{\kappa_s}{\kappa_f} = 123.5, \tag{15}$$

which are representative of water flowing within a steel pipe. The subscripts represent solid (*s*) and fluid (*f*), respectively. The density, Poisson ratio, thermal expansion and specific heat capacity of the solid are all selected based on C50 steel (EN 1.0540) as suggested by Cheng and Finnie (1996) for the TDSF simulations. The properties of the C50 steel are shown in Table 2.

Table 2

Properties of C50 steel (EN 1.0540) (Cheng and Finnie, 1996, Bringas, 2004, From, 2020).

Property	Unit	Value
Density	kg/m^3	7800
Poisson ratio	-	0.29
Thermal expansion coefficient	1/K	1.20×10^{-5}
Specific heat capacity	J/(kg·K)	470
Thermal diffusivity	m^2/s	1.84×10^{-5}
Thermal conductivity	W/(m·K)	83.98

2.5.Model Verification and Validation

The URANS results at $Fr = 0.670$ are compared with reference Large Eddy Simulation (LES) results (Skillen *et al.*, 2020) for the wall temperature and the velocity and has been presented in Zimoń *et al.* (2020), so is not repeated here. Good agreement has been observed that supports the accuracy of the URANS simulations.

The TDSF solver is validated against both 2-D and 3-D benchmark cases. The 2-D benchmark case is an analytical thermo-elastic case (Zander *et al.*, 2012). As shown in Figure 3 (a), a two-dimensional ring, with an outer radius of 1.0 m and inner radius of 0.25 m, has a prescribed temperature of 1 K and 3 K on the outer and inner boundary, respectively. The inner boundary of this ring is displaced by 0.25 m in the radial direction. The value of Young's modulus, coefficient of thermal expansion and thermal conductivity are all set to 1 in SI units. As can be seen from Figure 3(b)-(d), the differences between the present simulation results and the analytical results are less than 0.1% on the temperature distribution, displacement, and von-Mises stress, where the von-Mises stress is a criterion to assess the possibility of structural

damage (Segalman *et al.*, 2000) with the definition of:

$$\sigma_v = \sqrt{\frac{1}{2}[(\sigma_{11}-\sigma_{22})^2 + (\sigma_{22}-\sigma_{33})^2 + (\sigma_{33}-\sigma_{11})^2] + 3(\sigma_{12}^2 + \sigma_{23}^2 + \sigma_{31}^2)}, \quad (16)$$

where σ_{ij} is the Cauchy stress tensor. The 3-D benchmark case is a one-eighth hollow spherical vessel being heated and pressurised from its internal (Afkar *et al.*, 2014, Cardiff *et al.*, 2018). Figure 4 (a) presents the geometry and boundary conditions of the spherical vessel. The spherical vessel has an inner radius of 0.19 m and an outer radius of 0.2 m. The inner surface of the spherical vessel has a time varying temperature $T_{in} = 40t + T_{base}$ and pressure $P_{in} = t/5$, where t is the time and T_{base} is the base temperature that is 300 *K* in this case. The outer surface has a fixed surface convective heat coefficient h_{out}. Other thermal properties could be find from Cardiff *et al.* (2018). The von Mises Stress contour at $t = 5$ s is presented in Figure 4 (b). The von Mises Stress and temperature distributions along the radial direction are compared with published results in Figure 4 (c) and (d). Good agreement has been achieved.

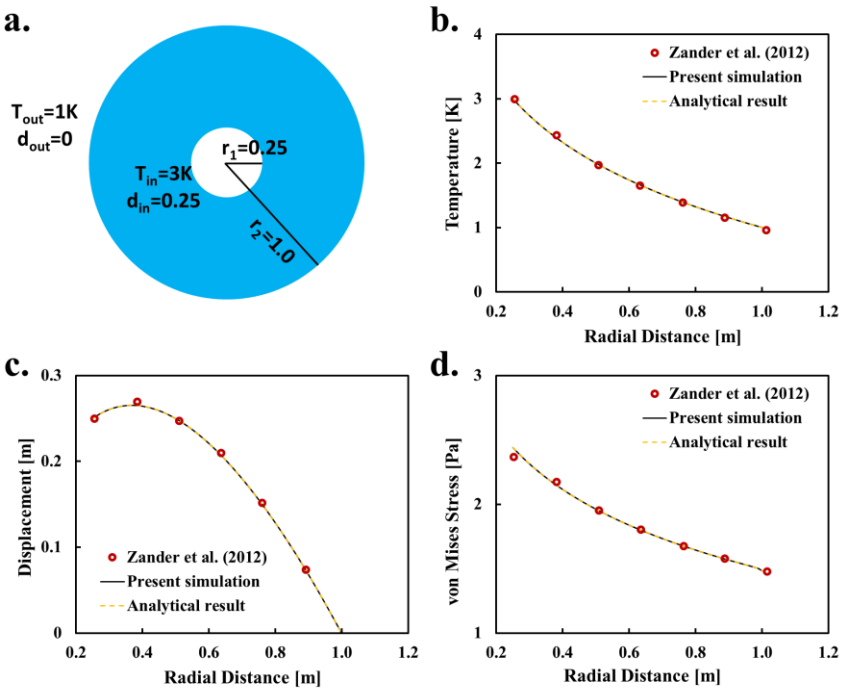

Figure 3. validation results of the solid mechanics code with 2-D benchmark case (Zander *et al.*, 2012).

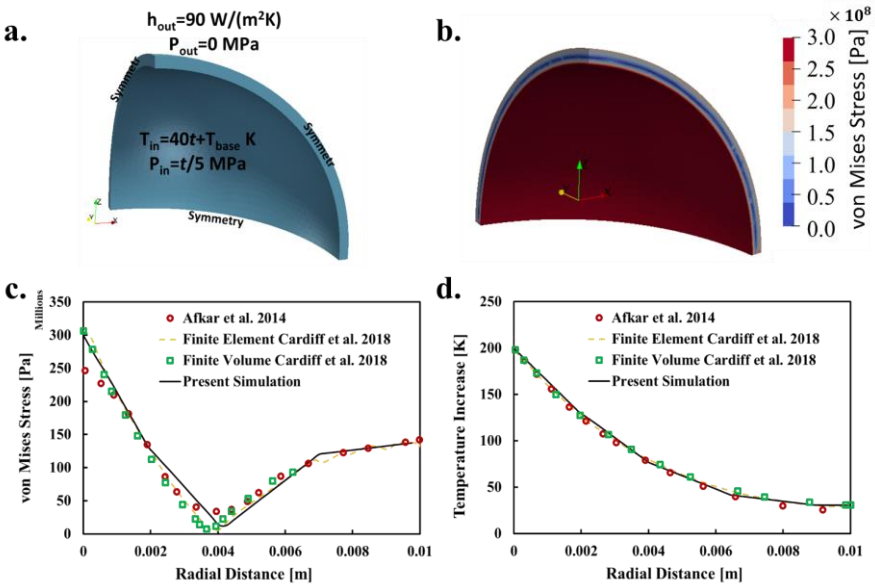

Figure 4. Validation results of the solid mechanics code with 3-D benchmark case (Afkar *et al.*, 2014, Cardiff *et al.*, 2018).

3. Results and Discussion

3.1. Thermal Flow and Conjugate Heat Transfer

Figure 5 shows a strong stratification in the thermal fluid with a large buoyancy-induced recirculation region in the fluid domain, which is similar to what is observed by Skillen *et al.* (2020). By investigating the fluid flow at the near-horizontal section, the classical Dean vortices are suppressed and a counter-rotating vortex pair formed when $\tilde{t} = 30$ as shown in Figure 6. This is due to the buoyancy effect between the cold dense near-wall fluid and the hot light fluid at the core of the pipe.

Figure 5. Flow streamline at $\tilde{t} = 15$ with $Fr = 0.670$, coloured by normalised temperature with yellow and blue indicate the high and low temperature, respectively.

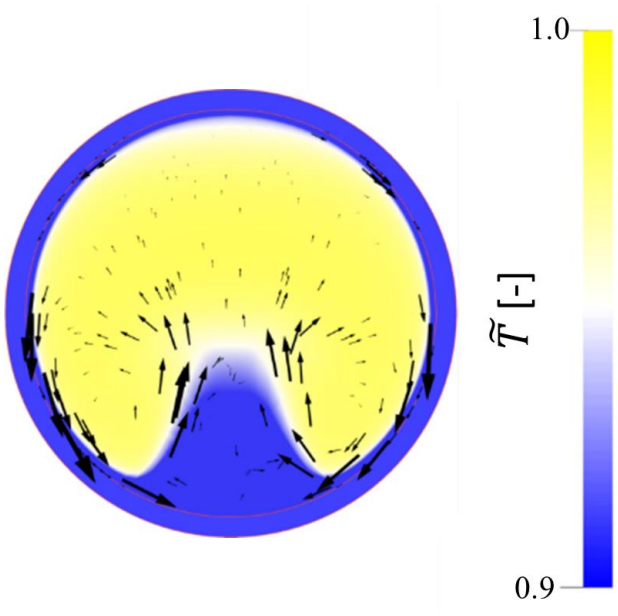

Figure 6. Secondary flow and temperature distribution at cross-sections through the near horizontal section ($x/D = 4.5$), at $\tilde{t} = 30$ with $Fr = 0.670$.

3.2. Wall Temperature Distribution

To investigate the effects of the stratification of the thermal fluid on the stress of the U-bend, the solid domain is focused on in the following sections.

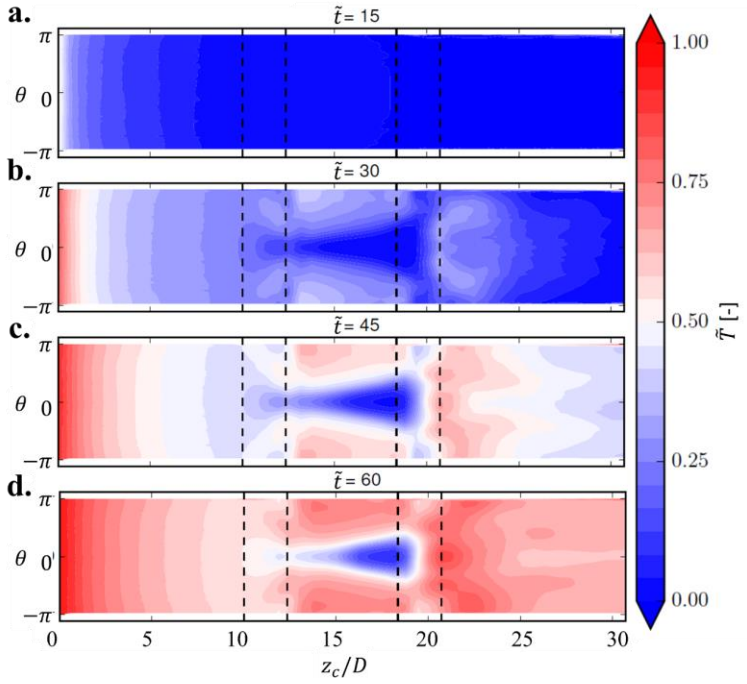

Figure 7. Flattened wall temperature contours at $\tilde{t} = 15$ (a), 30 (b), 45 (c) and 60 (d) with $Fr = 0.670$. Dashed lines indicated the locations of the two bends.

The wall temperature gradient is one of the most important sources of thermal stress. There is a positive correlation between pipe temperature gradient and thermal stress. For a given geometry, a larger temperature range within the solid domain typically leads to a steep temperature gradient. Figure 7 (a)-(d) show contours of normalised interface temperature, $\tilde{T} \equiv (T - T_0)/\Delta T$, at different $\tilde{t}$, and for $Fr = 0.670$ in a cylindrical coordinate system, where θ is the azimuth angle and z_c is the longitudinal location along the U-bend (the inlet of the domain is at $z_c/D = 0$). The two regions enclosed by the dashed lines are the locations of the bends. A thermal lag of the U-bend wall has been observed due to the thermal inertia as reported by Skillen *et al.* (2020). At $\tilde{t} = 15$, the thermal front has travelled to the near-horizontal section, while, as can be seen from Figure 7 (a), the upstream vertical section is still far below T_1. As time increases, both upstream and downstream vertical sections are gradually being heated by the thermal fluid. However, both of these sections have not fully reached T_1 until $\tilde{t} = 60$. A cold region at the bottom of the near-horizontal section can be observed from Figure 7 (b)–(d),

that is due to the stratification of the thermal fluid caused by the combination of the secondary flow and the recirculation. As time increases, the area of the stratification-induced cold region shrinks, but the temperature of the cold region does not undergo any major change.

The Froude number is a key condition to quantify the significance of the buoyancy effect over the flow inertia. With increasing Fr, the significance of the buoyancy effect reduces, which leads to a decrease of the strength of the secondary flow and a smaller of the recirculation region, hence the stratification is weaker in the fluid domain (Zimoń *et al.*, 2020). This phenomenon is reflected in the wall temperature, as shown in Figure 8 (a)-(c), which illustrates the contours of normalised temperature, $\tilde{T}$, with different Fr at $\tilde{t} = 60$ in a cylindrical coordinate system. It is worth to note that $\tilde{T}$ is calculated based on their respective ΔT for different Fr conditions. As can be seen, the core of the stratification-induced cold region is located around the joint between the near-horizontal region and the second bend for each Fr. For small Froude numbers, the cold region has a large area and a steep temperature gradient with its surrounding. The opposite is observed for larger Froude numbers. The spatial averaged temperature of the upstream vertical section has a positive correlation with the size of the cold region. In the range $Fr = 0.670$ and $Fr = 0.913$, a pair of hot regions appear, which are symmetrical about $\theta = 0$ in the downstream vertical section.

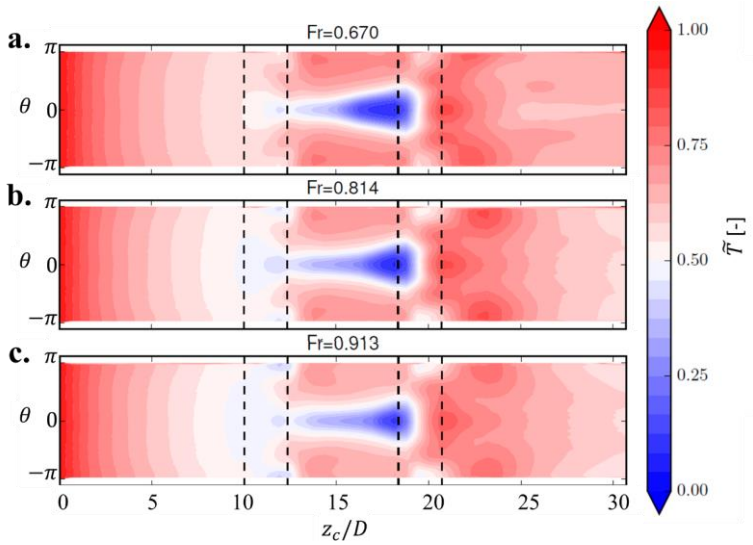

Figure 8. Flattened wall temperature contours with $Fr = 0.670$ (a), 0.814 (b) and 0.913 (c) at $\tilde{t} = 60$. Dashed lines indicate the locations of the two bends.

3.3. Thermally-Induced Displacement

Young's modulus is known to be a function of the temperature but is usually treated as a constant value if the variation of the temperature is small. In the present study, the temperature of the U-bend wall is much higher than the room temperature with a large temperature variation. Thus, the effect of the variation of Young's modulus with temperature needs to be investigated. In this work, the function of Young's modulus about temperature is estimated based on the polynomial fit of data from Engineering Toolbox (Engineering, 2004). Figure 9 (a) and (b) shows its contours at the U-bend wall at $\tilde{t} = 60$ with $Fr = 0.670$ and 0.913, respectively. When $Fr = 0.670$, the Young's modulus drops by 1.33% in the high temperature region close to the pipe inlet. While that is 0.87% when $Fr = 0.913$. The Lamé coefficients are determined by the Young's modulus, $E(T)$, as

$$\begin{cases} \lambda = \dfrac{E(T)\nu_s}{(1+\nu_s)(1+2\nu_s)}, \\ \mu = \dfrac{E(T)}{2+2\nu_s}, \end{cases} \tag{17}$$

where ν_s is the Poisson ratio. Based on equation (4), a 1.33% reduction of Young's modulus leads to a 1.33% reduction on each component of $\boldsymbol{\varepsilon_t}$ in the present working conditions.

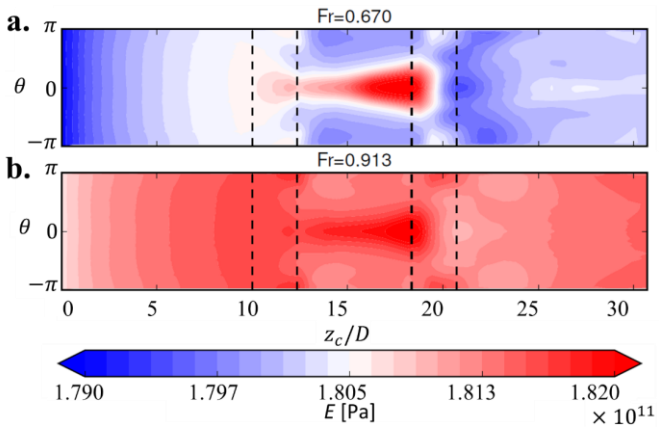

Figure 9. Young's modulus contour at $\tilde{t} = 60$ and $Fr = 0.670$ (a) and 0.913 (b).

The steel thermal conductivity is also a function of temperature, but the thermal conductivity changes a lot only when the temperature approaches absolute zero (Hahn and Özisik, 2012). In the present working condition, the thermal conductivity of steel is negatively correlated with the temperature. Its variation is between 1.37% and 0.67% (Powell *et al.*, 1966, Peet *et al.*, 2011, Hahn and Özisik, 2012) and the heat flux, according to Equation (6), has a 1.37% to 0.67% increment under the present working condition.

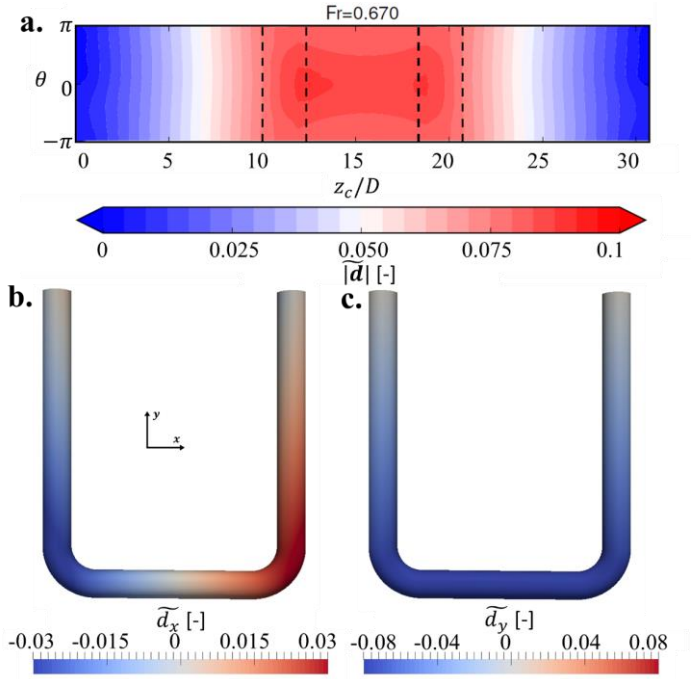

Figure 10. Thermal induced displacement contours at $\tilde{t} = 60$ and $Fr = 0.670$.

The contours of thermally-induced displacement at $\tilde{t} = 60$ and $Fr = 0.670$ are shown in Figure 10. As can be seen from Figure 10 (a), the junctions of bends and near-horizontal section exhibit the largest thermally-induced displacement. Figure 10 (b) and (c) show the x- and y-axis components of the thermally-induced displacement at $\tilde{t} = 60$ and $Fr = 0.670$. The maximum x-axis displacement of the U-bend is $0.070D$ located in the two bends. While the maximum y-axis displacement of the U-bend is $0.089D$ located in $z_c/D = 12.33$ and $\theta = 0$ (i.e. the horizontal section). Table 3 presents the maximum thermally-induced displacement magnitude over $\tilde{t}$ at $Fr = 0.670$. The displacement magnitude has an 3.67% increment from $\tilde{t} = 15$ to $\tilde{t} = 60$ as the wall is heated by the thermal fluid. The maximum thermally-induced displacement magnitude with different Fr at $\tilde{t} = 60$ have also been calculated. As shown in Figure 11, the thermally-induced displacement magnitude between $Fr = 0.670$ and $Fr = 0.913$ have a variation of $\Delta|\widetilde{d}|_{max} = 1.69 \times 10^{-3}$. This variation is the contributions from both the stratification-induced temperature gradients and the different ΔT at different Fr under the present working conditions.

Table 3

Maximum thermally-induced displacement components over time at $Fr = 0.670$.

$\tilde{t}$	$\lvert\widetilde{\boldsymbol{d}}\rvert_{max}$
[-]	[-]
15	8.53×10^{-2}
30	8.64×10^{-2}
45	8.77×10^{-2}
60	8.85×10^{-2}

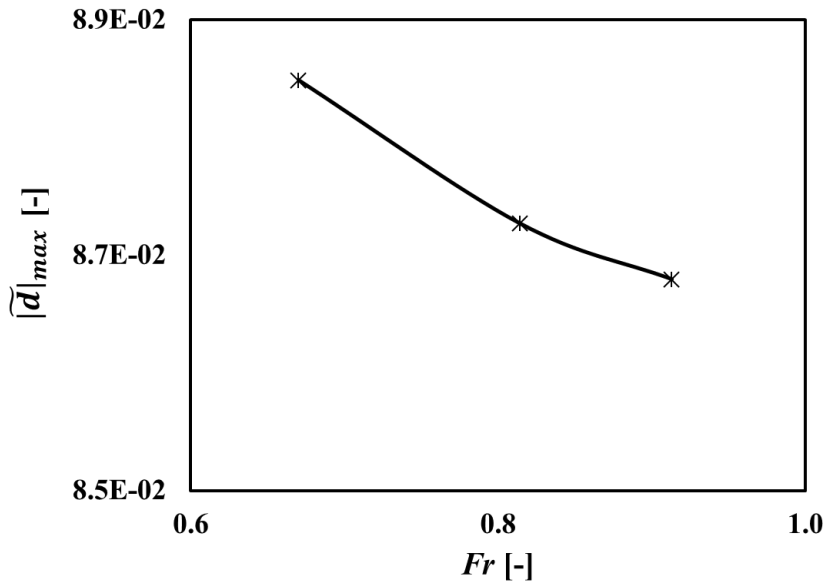

Figure 11. Maximum thermally-induced displacement magnitude v.s. Fr at $\tilde{t} = 60$.

As pointed by Kidawa-Kukla (2003) and Blandino and Thornton (2001), cyclic changes of temperature of a structure and non-uniform surface heating induce low frequency vibration. Time history of the displacement of the structure is an indication of the vibration. In order to investigate the thermally-induced vibration of the U-bend pipe under the present working conditions, several assumptions are needed to obtain the displacement time history. Since the present study considers the hot water injection only, we assume the cold-water injections could let the wall temperature of the U-bend return to its reference temperature, T_0 (i.e. a symmetrical hot-cold water injections). We also assume the U-bend pipe subject to indefinite cycles of the hot-cold water injections continuously. The profiles (includes the duration and the total temperature difference) of the hot-cold water injections among cycles are assumed to be the same. Figure 12 shows the time history of the thermally-induced displacement along *y*-axis direction at $Fr = 0.670$, $z_c/D = 12.33$ and $\theta = 0$. According to Figure 11, the thermally-induced displacement magnitude of the U-bend pipe at $Fr = 0.670$ has the highest value under the present working condition. As shown in Figure 10, $[z_c/D, \theta] = [12.33, 0]$ is the location of the maximum thermally-induced displacement along the pipe. By comparing between Figure

10 (b) and (c), the *y*-axis displacement is more pronounced than that of the *x*-axis displacement. Therefore, the displacement history shown in Figure 12 is the most pronounced one under the present working condition. As can be seen form Figure 12, a sinusoidal-like displacement history is obtained, which is qualitatively similar with Figure 2 (b) of the work of Kidawa-Kukla (2003). We observed that the frequency of the thermally-induced displacement is the same as the frequency of the hot-code water cycles. Moreover, the amplitude (difference between the peak and valley) of the vibration is only 0.74% of the pipe's diameter. Therefore, in the present working conditions and assumptions, the thermally-induced vibrations are limited to low frequency and small amplitude.

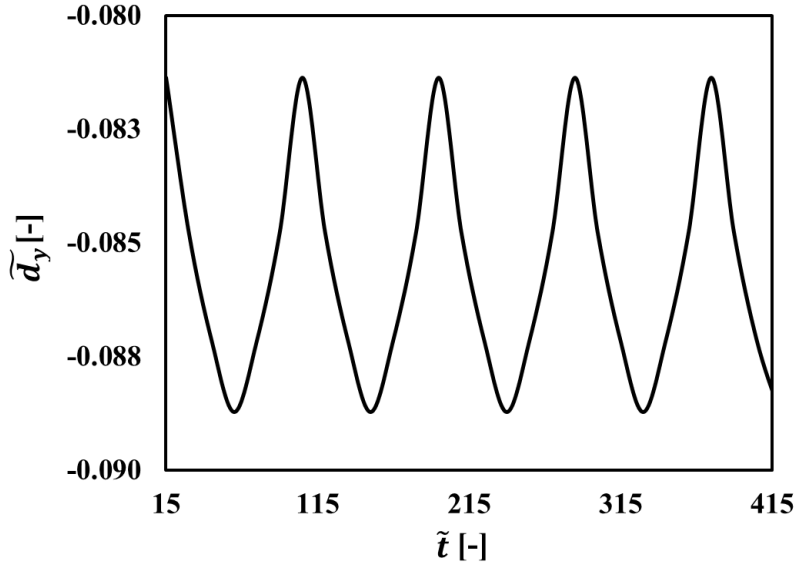

Figure 12. Thermally-induced displacement along *y*-axis direction in time domain at $Fr = 0.670$, $z_c/D = 12.33$ and $\theta = 0$.

In reality, the assumption may not apply, such as asymmetrical hot-cold water injections and/or the profiles of the hot-cold water injections among cycles are different. In that case, more site data is needed to carry out the thermally-induced vibration analysis. Apart from the thermally-induced vibration, there are also other sources of vibrations of the U-bend pipe, such as turbulence-induced vibration, thermal-hydraulic vibration due to the density difference for

instance (Blevins, 1990, Nakamura *et al.*, 2013, Miwa *et al.*, 2015), but these are out of the scope of the present study.

3.4.von-Mises Stress

The results of von-Mises stress are presented and analysed in this section. As shown in Figure 13 (a), the maximum stress is located at the two point-based displacement constraints, which is 3.84×10^9 Pa when $Fr = 0.670$ at $\tilde{t} = 60$. $3.84 \times 10^9 Fr = 0.670$ $\tilde{t} = 60$. It is about 39 times larger than the maximum stress at $z_c/D \in [5, 25]$ of the U-bend. The U-bend with ring-based displacement constraints (i.e. applying the displacement constraints to the entire circumferences of both the inlet and outlet boundaries) at $Fr = 0.670$ has also been simulated as a comparison. A large stress is observed at the entire circumferences for the ring-based constraints case. As can be seen from Figure 13 (a) and (b), the maximum stress of the ring-based constraints is about 22% smaller than that of the point-based constraints at $\tilde{t} = 60$. By applying the ring-based constraints, the stresses at the bends and the near-horizontal section have the same pattern but larger value compared with that of the point-based constraints, as illustrated in Figure 13 (c) and (d). As the boundary effect is out of the scope of this study, the simulations carried out in the following section are based on the point-based constraints. The stress discussed hereafter will focus on the U-bend for $z_c/D \in [5, 25]$ where there is less effect of the constraints.

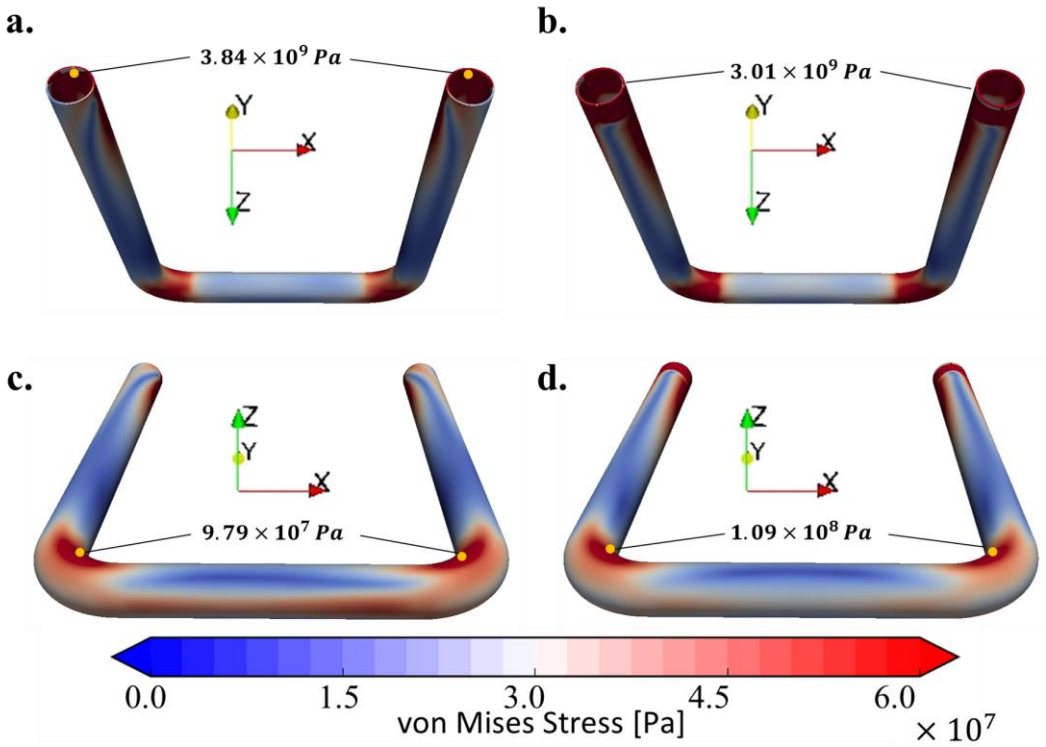

Figure 13. Contours of von-Mises stress with $Fr = 0.670$ at $\tilde{t} = 60$. (a) and (c) with point-based displacement constraints and (b) and (d) with ring-based displacement constraints.

The variation of the maximum von-Mises stress as a function of $\tilde{t}$ at $z_c/D \in [5, 25]$ is presented in Figure 14. The slope of the maximum σ_v is steep at $\tilde{t} < 30$, while there is only about 1% difference for the maximum σ_v between $\tilde{t} = 45$ and $\tilde{t} = 60$.

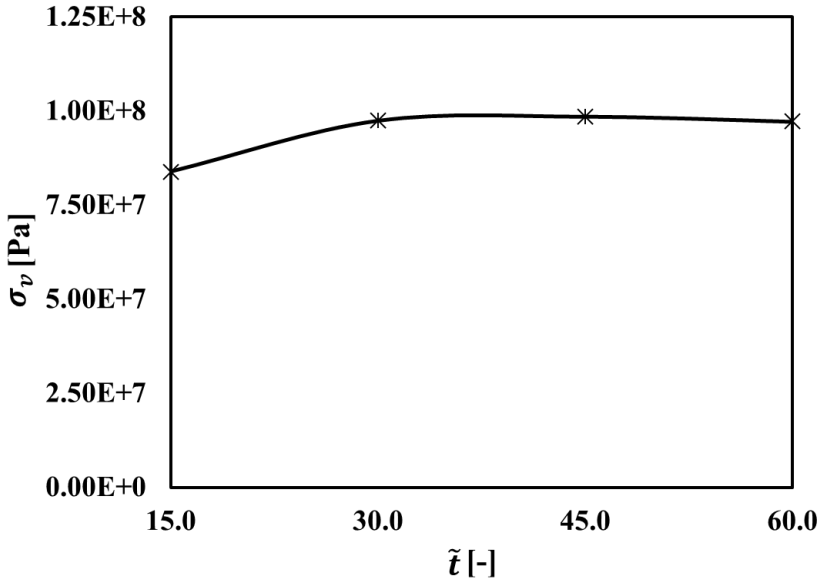

Figure 14. Maximum von-Mises stress at $z_c/D \in [5, 25]$ v.s. $\tilde{t}$ with $Fr = 0.670$.

The contours of thermally-induced von-Mises stress with different Froude numbers at $\tilde{t} = 60$ are shown in Figure 15. The thermal stress is believed to be a combined effect of the shape of the geometry, the temperature gradient of the U-bend wall and the different ΔT at different Fr. As can be seen, there are two types of areas subjected to large thermal stress. One is the front and back part of the two bends, as shown in Figure 13 (c). The other is the bottom of the near-horizontal section. By increase Fr from 0.670 to 0.913, a 4.03% reduction on the maximum von-Mises stress at $z_c/D \in [5, 25]$ can be identified. With an increase in Fr, the thermal stress decreases in these high-stress regions due to the decrease of the stratification-induced temperature gradients, as shown in Figure 8, and the decrease of ΔT.

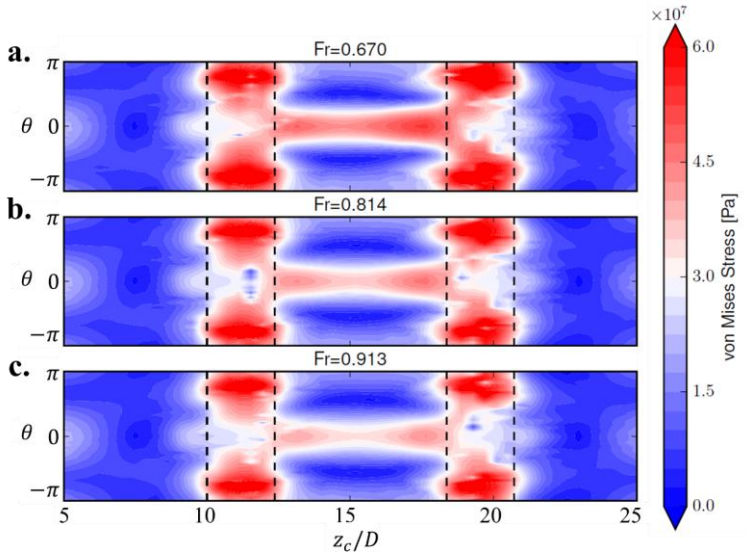

Figure 15. Contours of von-Mises stress at $z_c/D \in [5, 25]$ with $Fr = 0.670$ (a), 0.814 (b) and 0.913 (c) at $\tilde{t} = 60$.

3.5.Fatigue Life Prediction

The information of the full cycle, including the stress during the cold-water injections, is required to obtain an accurate fatigue life analysis of the U-bend. Due to a lack of data, the present study only gives a prediction following the procedure proposed by Cheng and Finnie

(1996), as in equations (7) to (9), by using the results of the thermally-induced stress, following the assumption that there is no denting present in the U-bend. According to Figure 14, the variation of the stress is small when $\tilde{t} \geq 45$. Therefore, the localised stress at $\tilde{t} = 60$ is used as the localised total stress of equation (8). The second assumption is symmetrical hot-cold water injections. Thus, the localised mean stress, σ_m^i, is calculated based on the stress of the U-bend at T_0 and σ_a^i.

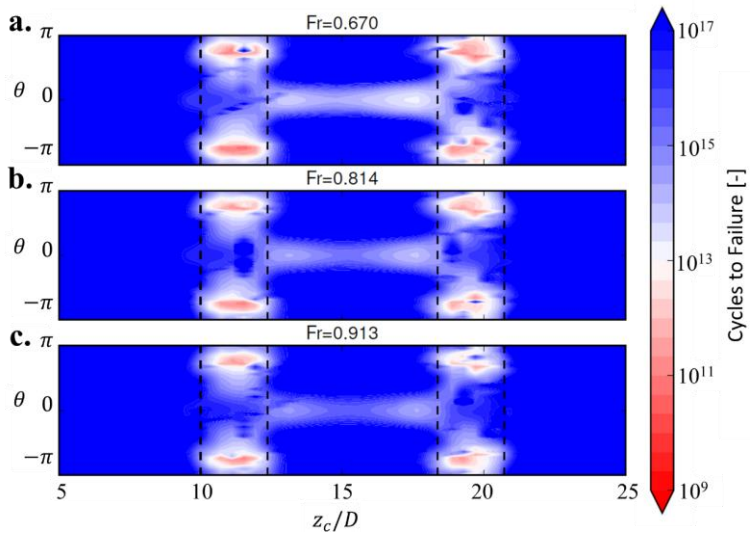

Figure 16. Fatigue life contours with $Fr = 0.670$ (a), 0.814 (b) and 0.913 (c).

With the present working conditions and assumptions, the contours of the cycles to failure with different Froude numbers are shown in Figure 16. It can be seen that the patterns of fatigue contours are close to that of the stress contours in Figure 15 since a larger stress leads to a smaller number of cycles to failure. The weakest part of the U-bend is at the front and back part of the two bends. With an increase of Fr, the number of cycles to failure increases, i.e. the U-bend is predicted to last longer. Figure 17 plots the minimum number of cycles to failure for different Fr. It can be seen that the minimum number of cycles to failure drops from 6.39×10^{10} to 2.18×10^{10} when Fr decreases from 0.913 to 0.670, i.e. the pipe is easier to break at a lower Fr, under the present working condition.

It is worth noting that denting, caused by the interaction between the U-bend and its supporting structures, has a significant influence on the fatigue life and reduces the cycles to failure by about four orders of magnitude, according to the study of Cheng and Finnie (1996). As applying supporting structures to the U-bend is essential in reality, a much shorter fatigue life than that in Figure 17 with the presence of dents in the U-bend should be expected.

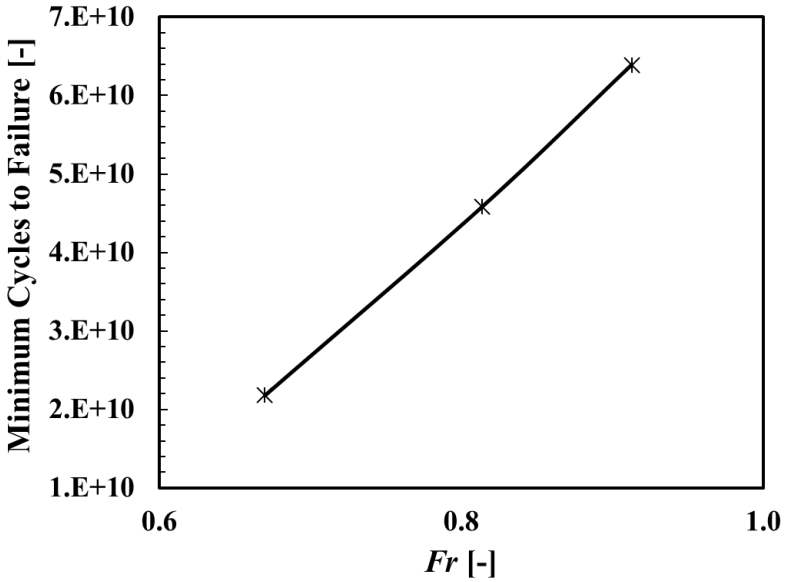

Figure 17. Minimum cycles to failure v.s. Fr.

3.6.Infinite Froude number

As discussed in previous sections, both stratification-induced temperature gradients and ΔT have contributed to the Froude number effect. In order to identify the influence of the thermal stratification to the thermal stress, a set of idealised cases have been designed. In this set of cases, the temperature difference is fixed as $\Delta T = 38°C$ and the gravitational acceleration varies to act on the Froude numbers going from 0.670 to 0.913. Moreover, the gravitational acceleration has been further reduced to zero (i.e. $Fr = \infty$) and assume the thermal fluid has flowed long enough so that the gradient of the U-bend wall temperature equals zero everywhere. Figure 18 shows the contour of the von-Mises stress at $z_c/D \in [5, 25]$ with five

Froude numbers at $\tilde{t} = 60$ under fixed ΔT condition. Since the temperature gradient equals zero across the whole domain, the thermally-induced stress shown in Figure 18 (d) is purely a contribution from the shape of the geometry. The difference between Figure 18 (d) and Figure 18 (a)-(c) are the contributions from the stratification of the thermal fluid. It can be seen that the stratification of the thermal fluid increases the thermal stress at the front and back part of the two bends and generates a large stress region at the bottom of the near-horizontal section. With the combined effect of the geometry and the temperature gradient, the front and back parts of the bends are subject to the highest stress of the U-bend. Table 4 lists the maximum von-Mises stress with different Fr at $\tilde{t} = 60$ under fixed ΔT condition. A 3.4% increment can has been observed on the stress at $Fr = 0.427$ compared with that of $Fr = \infty$. This indicates that the stratification-induced temperature gradients have an important effect on the stress of the U-bend.

Table 4

Maximum von-Mises stress at $z_c/D \in [5, 25]$ with different Fr at $\tilde{t} = 60$ under fixed ΔT condition.

Fr [-]	Maximum von-Mises stress [Pa]	Increase rate [%]
0.670	9.72×10^7	13.12
0.814	9.50×10^7	10.55
0.913	9.33×10^7	8.56
∞	8.59×10^7	0.00

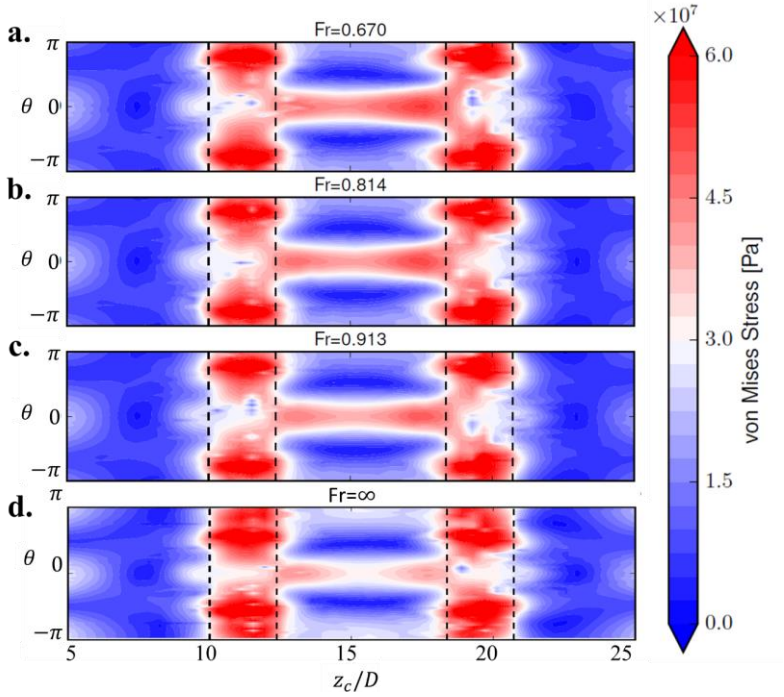

Figure 18. Contours of von-Mises stress at $z_c/D \in [5, 25]$ with $Fr = 0.670$ (a), 0.814 (b), 0.913 (c) and ∞ (d) at $\tilde{t} = 60$ under fixed ΔT condition.

4. Conclusions

A coupled framework was used to simulate the conjugate heat transfer between the fluid and solid walls and the corresponding thermal stress of a U-bend. Results highlight the complex flow evolution. Significantly, a reversal of the Dean vortex pair due to buoyancy occurs. Steep wall temperature gradients have been observed due to buoyancy-induced stratification. We observed low frequency and small amplitude thermally-induced vibrations under the present working conditions. Wall temperature gradients and wall thermal stress have negative correlations with the value of Fr. The maximum von-Mises stress has a 4.03% reduction due to the combined effect of the stratification-induced temperature gradients and the ΔT. The stress has an up to 3.4% increment under the present working conditions due to thermally-induced temperature gradients only. A fatigue life estimation is also carried out by using the thermal stress data through an empirical formula. It indicates that the weakest parts of the U-

bend are the front and back parts of the two bends. Moreover, results indicate that the buoyancy-induced stratification of the thermal fluids increases the thermal stress at the front and back part of the two bends and generates a large stress region at the bottom of the near-horizontal section, which can reduce the operational life of the U-bend.

The present study established a coupled framework between the Finite Volume CHT solver and the Finite Element thermal-elasticity solver. It enables the simulation of thermal-elasticity related multi-physical phenomenon involved in the nuclear industry for a safer design. One-way coupling from the CHT solver to the thermal-elasticity solver is used in the present study, as the thermally induced displacement is relatively small. In the near future, the solver will be further extended to enable two-way couplings between CHT and thermal-elasticity solvers so that to simulate thermal-elastic phenomenon with large displacement. The Finite Element based fatigue life prediction method should be implemented in the near future to replace the present empirical formula for a high accuracy.

Nomenclature

b applied mechanical volume load

$\boldsymbol{C}$ constitutive tensor

$\boldsymbol{d}$ displacement vector

$\tilde{\boldsymbol{d}}$ dimensionless displacement

D pipe's diameter

$\boldsymbol{\Theta}$ displacement admissible function space

Dn Dean number

$E(T)$ Young's modulus as a function of temperature

Fr Froude Number

g gravitational acceleration (m/s^2)

$\boldsymbol{I}$ identity matrix

k thermal conductivity

N cycles to failure

$\boldsymbol{q}$ heat flux

R_c radius of curvature

Re Reynolds number based on the pipe's diameter

s entropy per unit of mass

t time (s)

$\tilde{t}$ dimensionless time

T temperature distribution

$\widehat{ta}$ prescribed traction on the solid boundary

$tr(a)$ trace of matrix a

U bulk flow velocity (m/s)

z_c longitudinal location of the U-bend

Greek symbols

α thermal diffusivity

β expansion coefficient

$\boldsymbol{\Gamma}$ boundary of the domain

δ increment of a given variable

Δ difference of a given variable

$\boldsymbol{\varepsilon}$ strain tensor

θ thermal conductivity

κ thermal conductivity

λ the second Lamé coefficients

μ the first Lamé coefficients

ν kinematic viscosity

ν_s Poisson ratio

ρ density

$\boldsymbol{\sigma}$ stress tensor

σ_v von-Mises stress

$\boldsymbol{\Omega}$ physical domain

Subscripts

0 initial value

1 final value

a combining the mean and purely alternating

f fluid

m mean alternating

max maximum value

pa purely alternating

s solid

t thermal

u ultimate

x x-axis component

y y-axis component

z z-axis component

Superscripts

i the i^{th} element of localised variable

Abbreviations

CHT Conjugate heat transfer

EBRSM Elliptic Blending Reynolds-Stress Model

LES Large Eddy Simulation

TDSF The Thermal Displacement, Stress analysis, and Fatigue life prediction

URANS Unsteady Reynolds Averaged Navier-Stokes

Acknowledgement

This work was supported by the STFC Hartree Centre's Innovation Return on Research programme, funded by the Department for Business, Energy & Industrial Strategy. Computational time on ARCHER, the UK National Supercomputing Service (http://www.archer.ac.uk), was provided through the UK Turbulence Consortium, under grant number EP/R029326/1. We further thanks the Engineering and Physical Science Research Council for their support under projects EP/R029369/1 and EP/N016602/1.

References

Afkar, A., Camari, M. N., and Paykani, A., Design and analysis of a spherical pressure vessel using finite element method. *World Journal of Modelling and Simulation*, vol. **10**, no. 2, pp. 126-135, 2014.

Alnæs, M., Blechta, J., Hake, J., Johansson, A., Kehlet, B., Logg, A., Richardson, C., Ring, J., Rognes, M. E., and Wells, G. N., The FEniCS project version 1.5. *Archive of Numerical Software*, vol. **3**, no. 100, 2015.

Attia, M. H., Fretting fatigue and wear damage of structural components in nuclear power stations—Fitness for service and life management perspective. *Tribology International*, vol. **39**, no. 10, pp. 1294-1304, 2006.

Blandino, J. R., and Thornton, E. A., Thermally induced vibration of an internally heated beam. *J. Vib. Acoust*, vol. **123**, no. 1, pp. 67-75, 2001.

Blevins, R., Flow induced vibration Second edition. *Florida, Krieger Publishing Co*, 1990.

Bleyer, J., Numerical Tours of Computational Mechanics with FEniCS. *Zenodo. http://doi.org/10.5281/zenodo.1287832*, 2018.

Blumm, J. and Lindemann, A., Characterization of the thermophysical properties of molten polymers and liquids using the flash technique. *High Temp. High Press*, vol. **35**, no. 36, pp. 627-627, 2003.

Bringas, J. E., *Handbook of comparative world steel standards*, ASTM International, 2004.

Cardiff, P., Karač, A., De Jaeger, P., Jasak, H., Nagy, J., Ivanković, A., and Tuković, Ž., An open-source finite volume toolbox for solid mechanics and fluid-solid interaction simulations. *arXiv preprint arXiv:1808.10736*, 2018.
Cheng, W., and Finnie, I., Stress analysis and fatigue life prediction for a U-bend steam generator tube. *Nuclear engineering and design*, vol. **165**, no. 1-2, pp. 101-109, 1996.
Daly, B. J., and Harlow, F. H., Transport equations in turbulence. *The Physics of Fluids*, vol. **13**, no. 11, pp. 2634-2649, 1970.
Durmayaz, A., and Yavuz, H., Exergy analysis of a pressurized-water reactor nuclear-power plant. *Applied energy*, vol. **69**, no. 1, pp. 39-57, 2001.
Engineering, T., Water - Density, Specific Weight and Thermal Expansion Coefficient, 2003.
Engineering, T., Water - Dynamic and Kinematic Viscosity, 2004.
Engineering, T., Young's Modulus of Elasticity for Metals and Alloys., 2004.
Fatemi, A., and Yang, L., Cumulative fatigue damage and life prediction theories: a survey of the state of the art for homogeneous materials. *International journal of fatigue*, vol. **20**, no. 1, pp. 9-34, 1998.
Flores, O., Marugán-Cruz, C., Santana, D., and García-Villalba, M., Thermal stresses analysis of a circular tube in a central receiver. *Energy Procedia*, vol. **49**, pp. 354-362, 2014.
Fournier, Y., Massively Parallel Location and Exchange Tools for Unstructured Meshes. *International Journal of Computational Fluid Dynamics*, pp. 1-20, 2020.
Fournier, Y., Bonelle, J., Moulinec, C., Shang, Z., Sunderland, A., and Uribe, J., Optimizing Code_Saturne computations on Petascale systems. *Computers & Fluids*, vol. **45**, no. 1, pp. 103-108, 2011.
From, M., EN 1.0540 (C50) Non-Alloy Steel., *Makeitfrom.com.*, 2020.
Giannakopoulos, G., Frouzakis, C. E., Boulouchos, K., Fischer, P. F., and Tomboulides, A., Direct numerical simulation of the flow in the intake pipe of an internal combustion engine. *International Journal of Heat and Fluid Flow*, vol. **68**, pp. 257-268, 2017.
Goodman, J., *Mechanics applied to engineering*, Longmans, Green, 1919.
Green, S., and Hetsroni, G., PWR steam generators. *International journal of multiphase flow*, vol. **21**, pp. 1-97, 1995.
Hahn, D. W., and Özisik, M. N., *Heat conduction*, John Wiley & Sons, 2012.
Ince, N., and Launder, B., On the computation of buoyancy-driven turbulent flows in rectangular enclosures. *International Journal of Heat and Fluid Flow*, vol. **10**, no. 2, pp. 110-117, 1989.
Jacko, R., Fatigue Performance of Ni–Cr–Fe Alloy 600 Under Typical PWR Steam Generator Conditions. *Electric Power Research Institute, Palo Alto, CA, Report No. EPRI NP-2957*, 1983.
Kidawa-Kukla, J., Application of the Green functions to the problem of the thermally induced vibration of a beam. *Journal of sound and vibration*, vol. **262**, no. 4, pp. 865-876, 2003.
Langtangen, H. P., A FEniCS tutorial. *Automated Solution of Differential Equations by the Finite Element Method*, Springer, pp. 1-73, 2012.
Manceau, R., and Hanjalić, K., Elliptic blending model: A new near-wall Reynolds-stress turbulence closure. *Physics of Fluids*, vol. **14**, no. 2, pp. 744-754, 2002.
Marugán-Cruz, C., Flores, O., Santana, D., and García-Villalba, M., Heat transfer and thermal stresses in a circular tube with a non-uniform heat flux. *International Journal of Heat and Mass Transfer*, vol. **96**, pp. 256-266, 2016.
Miwa, S., Mori, M., and Hibiki, T., Two-phase flow induced vibration in piping systems. *Progress in Nuclear Energy*, vol. **78**, pp. 270-284, 2015.
Nair, P. P., and Gopal, M., Sensitivity-reduced design for a nuclear pressurized water reactor. *IEEE transactions on nuclear science*, vol. **34**, no. 6, pp. 1834-1842, 1987.

Nakamura, T., Kaneko, S., Inada, F., Kato, M., Ishihara, K., Nishihara, T., Mureithi, N. W., and Langthjem, M. A., *Flow-induced vibrations: classifications and lessons from practical experiences*, Butterworth-Heinemann, 2013.
Noorani, A., Khoury G. E., and Schlatter, P., Evolution of turbulence characteristics from straight to curved pipes. *International journal of heat and fluid flow*, vol. **41**, pp. 16-26, 2013.
Peet, M., Hasan, H., and Bhadeshia, H., Prediction of thermal conductivity of steel. *International Journal of Heat and Mass Transfer*, vol. **54**, no. 11-12, pp. 2602-2608, 2011.
Powell, R., Ho, C. Y., and Liley, P. E., *Thermal conductivity of selected materials*, US Department of Commerce, National Bureau of Standards Washington, DC, 1966.
Prevéy, P. S., Surface residual stress distributions in as-bent Inconel 600 U-bend and Incoloy 800 90-degree bend tubing samples. *Workshop Proceedings: U-Bend Tube Cracking in Steam Generators*, EPRI, Palo Alto, CA, 1981.
Rodríguez-Sánchez, M. R., Marugan-Cruz, C., Acosta-Iborra, A., and Santana, D., Comparison of simplified heat transfer models and CFD simulations for molten salt external receiver. *Applied thermal engineering*, vol. **73**, no. 1, pp. 993-1005, 2014.
Schwartz, M. P., Four types of heat exchanger failures. *ITT Bell & Gosset*, 1982.
Segalman, D., Reese, G., Field, J. R., and Fulcher, C., Estimating the probability distribution of Von Mises stress for structures undergoing random excitation. *J. Vib. Acoust.*, vol. **122**, no. 1, pp. 42-48, 2000.
Skillen, A., Zimoń, M., Sawko, R., Tunstall, R., Moulinec, C., and Emerson, D. R., Thermal transients in a U-bend. *International Journal of Heat and Mass Transfer*, vol. **148**, pp. 11-39, 2020.
Tunstall, R., Laurence, D., Prosser, R., and Skillen, A., Benchmarking LES with wall-functions and RANS for fatigue problems in thermal–hydraulics systems. *Nuclear Engineering and Design*, vol. **308**, pp. 170-181, 2016.
Vashisth, S., Kumar, V., and Nigam, K. D., A review on the potential applications of curved geometries in process industry. *Industrial & Engineering Chemistry Research*, vol. **47**, no. 10, pp. 3291-3337, 2008.
Viollet, P., Observation and numerical modelling of density currents resulting from thermal transients in a non rectilinear pipe. *Journal of Hydraulic Research*, vol. **25**, no. 2, pp. 235-261, 1987.
Zander, N., Kollmannsberger, S., Ruess, M., Yosibash, Z., and Rank, E., The finite cell method for linear thermoelasticity. *Computers & Mathematics with Applications* vol. **64**, no. 11, pp. 3527-3541, 2012.
Zimoń, M. J., Skillen, A., Liu, W., and Sawko, R., Surrogate modelling of transient stratified flow in a u-shaped pipe. *Nuclear Engineering and Design*, vol. **368**, 2020.